

Article

Entropy Production Evaluation within a Prototype Pump-Turbine Operated in Pump Mode for a Wide Range of Flow Conditions

Xiaotong Yan ¹, Kan Kan ^{1,2,*}, Yuan Zheng ¹, Huixiang Chen ^{2,3}  and Maxime Binama ⁴ ¹ College of Energy and Electrical Engineering, Hohai University, Nanjing 211100, China² College of Water Conservancy and Hydropower Engineering, Hohai University, Nanjing 210098, China³ College of Agricultural Science and Engineering, Hohai University, Nanjing 211100, China⁴ College of Petroleum Engineering, Liaoning Petrochemical University, Fushun 113005, China

* Correspondence: kankan@hhu.edu.cn

Abstract: Inside the pump-turbine, energy is irreversibly lost due to turbulent pulsations in the high Reynolds number zone and actions of viscous forces close to the wall. The conventional differential pressure method cannot obtain specific details of the hydraulic loss within the machine's flow passages; on the other hand, the entropy production method can provide accurate information on the location of irreversible losses and the spatial distribution of energy dissipation. Therefore, based on the entropy production theory, this study investigates the composition and distribution of hydraulic losses under different flow conditions for a prototype pump-turbine in pump mode. Study results indicated that total hydraulic losses significantly decreased, then slowly increased with an increase in flow rate. The entropy production rate caused by turbulence dissipation (EPTD), direct dissipation (EPDD), and wall shear stress (EPWS) displayed the same variation patterns as that of total hydraulic losses, with EPTD and EPDD being the most dominating. The location of hydraulic loss within the pump-turbine's flow domain strongly depended on flow conditions. High hydraulic losses primarily occurred in the guide vanes (GV) and draft tube under low flow rates. Under high flow conditions, however, high hydraulic losses were mostly concentrated in the stay vanes (SV), spiral casing, and GV. Hydraulic losses at low flow rates were primarily caused by flow separation within the GV flow channels, vortices in the vaneless region, and inlet flow impacts on the runner blade's leading edge. On the other hand, large vortices within the GV and SV flow channels, GV wake flow, and unsteady flow at the spiral casing were the main contributors to hydraulic loss under high flow conditions. EPDD was mainly caused by strain rate, so it was closer to the main vortex regions, whereas EPTD was affected by turbulence intensity and had a wider distribution range in the unsteady flow.

Keywords: pump-turbine; pump mode; entropy production; hydraulic loss; various operating conditions



Citation: Yan, X.; Kan, K.; Zheng, Y.; Chen, H.; Binama, M. Entropy Production Evaluation within a Prototype Pump-Turbine Operated in Pump Mode for a Wide Range of Flow Conditions. *Processes* **2022**, *10*, 2058. <https://doi.org/10.3390/pr10102058>

Academic Editor: Blaž Likozar

Received: 2 October 2022

Accepted: 10 October 2022

Published: 12 October 2022

Publisher's Note: MDPI stays neutral with regard to jurisdictional claims in published maps and institutional affiliations.



Copyright: © 2022 by the authors. Licensee MDPI, Basel, Switzerland. This article is an open access article distributed under the terms and conditions of the Creative Commons Attribution (CC BY) license (<https://creativecommons.org/licenses/by/4.0/>).

1. Introduction

With the globally rising energy demand, fossil fuels are becoming depleted as the main energy source due to continual exploitation. Simultaneously, the vast amounts of carbon dioxide and harmful gases produced by fossil fuel consumption contributes to global warming and environmental pollution problems such as acid rain. Therefore, a worldwide agreement has emerged to significantly raise the amount of clean and renewable energy. However, the electricity produced from solar and wind energy is random, inconsistent, and unstable. When these energy sources are connected to the power system on a large scale, they may have a significant impact on its security and stability. The most effective solution to this is to adopt large-scale energy storage technology for regulation. Pumped storage, as the most mature and successful method of energy storage, has the ability to rapidly start and stop and flexibly regulate energy storage, making it an excellent method for controlling

the power instabilities caused by a high penetration of other renewable energies within the power grid.

As the core component of energy conversion in a pumped storage power station, the pump-turbine is a special form of hydraulic machinery, integrating the functions of a pump and a hydraulic turbine [1]. Pump-turbine hydraulic performance analysis methods include model experiments and numerical simulations [2–4]. Li et al. [5] studied the hysteresis characteristic of a model pump-turbine in pump mode through model experiments. Lu et al. [6] carried out experiments to investigate cavitation influences on pump performance characteristics of a low specific speed model pump-turbine. Sun et al. [7] performed experimental investigations on pressure pulsation characteristics of a prototype pump-turbine in the start-up process. Due to experimental limitations, experimental investigations of pump-turbine models are generally limited to the measurement and analysis of external performance characteristics. Although the development and application of special observation techniques, such as particle image velocimetry (PIV), can greatly enhance measurement accuracy, the local characteristics of the flow field are still not well-observed. On the other hand, numerical simulations can reveal more detailed information on the flow field, and numerous scholars have carried out numerical research on various types of hydraulic machinery [8–10]. Among the numerical studies conducted on pump-turbines in pump mode, Wang et al. [11] studied the application of entropy production theory to cavitation flow in a pump-turbine under pump mode. Wang et al. [12] investigated how a pump turbine's transient characteristics could be affected by the guide vane closing pattern. Tao et al. [13] carried out research on energy dissipation properties of the pump-turbine.

The recent high penetration of renewable energies (wind and solar energy) into the power grid has led to serious power supply instabilities. To cope with these instabilities, pump-turbines in connected pumped-storage power plants are subject to frequent start-stops, shifts between pump and turbine operating modes, and off-design operating conditions for most of their operating time. Therefore, pump-turbines are required to have a wide range of stable operating conditions. Under off-design operating conditions, the flow velocity within the machine's flow channels substantially vary and are not uniformly distributed. Furthermore, viscous forces near the wall and turbulent pulsations in the high Reynolds number zone cause irreversible hydraulic losses inside the pump-turbine. Hydraulic loss has always been a popular research topic [14,15]. Differential pressure method and entropy production method are two of the most utilized hydraulic loss assessment methods for hydraulic machinery. The differential pressure method is based on calculations using the energy conservation equation, which calculates the energy difference between the intake and outlet of each flow component to determine the value of its hydraulic losses. The conventional differential pressure method cannot identify specific details of the hydraulic loss within each component. The entropy production method, on the other hand, reflects the location of irreversible losses within the flow field, as well as the spatial distribution of energy consumption [16–18]. The extracted information strongly contributes to improvements in pump-turbine performance and hydraulic optimization. In recent years, an increasing number of scholars have applied entropy production theory to studies on hydraulic machinery. Gong et al. [19] first applied the entropy production theory to the hydraulic loss analysis of hydraulic machinery, where it was shown that the use of entropy production analysis could pinpoint the location of high losses, providing a theoretical basis for hydraulic optimization. Hou et al. [20] evaluated hydraulic loss in centrifugal pumps using the entropy production method and verified that the hydraulic losses calculated using the entropy production method were consistent with the results from the conventional differential pressure method. Li et al. [21,22] adopted the entropy production theory and revealed that the pump turbine's hump and hysteresis characteristics mainly originate from the hydraulic losses caused by the backflow at the runner inlet near the band casting, as well as the flow separation vortices in guide and stay vane flow channels. These studies indicated that entropy production theory has obvious advantages in hydraulic loss assessment and can accurately identify specific locations where these losses take place. However,

few studies on the hydraulic performance analysis of pump-turbines have utilized entropy production theory.

Therefore, this study adopted the entropy production theory to quantify and locate the scale and location of hydraulic losses within a prototype pump-turbine, and assess the hydraulic loss mechanism under different flow conditions. This study makes three innovative contributions to the literature: (1) Based on the entropy production theory, we thoroughly analyzed the composition and distribution of the pump-turbine's hydraulic losses in pump mode. (2) We reveal the variation and mechanism of hydraulic loss under different flow conditions in pump mode. (3) The correlations between the large-scale vortex, flow separation, rotational stall speed, and pump-turbine hydraulic losses were analyzed. This paper is organized as follows: The utilized numerical method, entropy production theory, as well as the geometric characteristics of the studied pump-turbine model are presented in Section 2. Analysis and discussion of the simulation results, including the validation of the adopted numerical simulation scheme, analysis of hydraulic loss compositions, and distribution within different components of the computational domain, are presented in Section 3. Finally, Section 4 presents the conclusions of the study.

2. Methodology and Numerical Model

2.1. Governing Equations and Turbulence Model

When considering an incompressible fluid, the pump-turbine's steady flow follows the continuity and momentum equations, whose mathematical expressions are shown in Equations (1) and (2).

$$\frac{\partial(\bar{u}_i)}{\partial x_i} = 0 \quad (1)$$

$$\frac{\partial(\rho\bar{u}_i)}{\partial t} + \frac{\partial(\rho\bar{u}_i\bar{u}_j)}{\partial x_j} = -\frac{\partial\bar{p}}{\partial x_i} + \frac{\partial}{\partial x_j} \left(\mu \frac{\partial\bar{u}_i}{\partial x_j} \right) - \frac{\partial\tau_{ij}}{\partial x_j} \quad (2)$$

In these equations, \bar{u}_i and \bar{u}_j are the components of the time-averaged velocity; x_i and x_j represent the Cartesian coordinate components; ρ is the density; t is the physical time; \bar{p} denotes the time-averaged pressure; μ presents the dynamic viscosity; and τ_{ij} presents the subgrid-scale stress.

The motion of an incompressible viscous fluid can be described by the Navier–Stokes equation:

$$\rho \frac{D\vec{v}}{Dt} = \rho \vec{f} - \nabla \vec{p} + \mu \nabla^2 \vec{v} \quad (3)$$

Theoretically, all turbulence scales and flow structures of the flow field can be captured by solving the N–S equation. However, due to the complexity of the actual flow, it is hard to obtain the exact solution of the flow field by simply solving the N–S equation. According to the requirements for the accuracy and scale of the turbulent pulsation solution, numerical computation methods for solving turbulence are divided into three main categories [23]: direct numerical simulation (DNS), large eddy simulation (LES), and Reynolds time-averaged numerical simulation (RANS). In particular, the RANS method is obtained by a Reynolds time averaging of the Navier–Stokes equation, which decomposes the flow into a time-averaged flow and transient pulsating flow. The governing equation will have an additional unknown Reynolds stress term, $-\rho m \langle \vec{u}'_i \vec{u}'_j \rangle$, after the time homogenization treatment. Based on Boussinesq's hypothesis, the relationship between the Reynolds stress and the time-averaged velocity gradient in the flow field can be established using the vortex viscosity coefficient:

$$-\rho m \langle \vec{u}'_i \vec{u}'_j \rangle = \mu_t \left(\frac{\partial \langle \vec{u}_i \rangle}{\partial x_j} + \frac{\partial \langle \vec{u}_j \rangle}{\partial x_i} \right) - \frac{2}{3} \mu_t \delta_{ij} \frac{\partial \langle \vec{u}_k \rangle}{\partial x_k} - \frac{2}{3} \rho_m k \delta_{ij} \quad (4)$$

where $\langle \cdot \rangle$ denotes the time-averaged value. Depending on the number of transport equations constructed to solve the turbulent viscosity coefficients, they can be divided into zero-equation models, single-equation models, and two-equation models.

For the SST k - ω dual equation turbulence model, the k equation is denoted as:

$$\frac{\partial(\rho k)}{\partial t} + \frac{\partial(\rho \bar{u}_j k)}{\partial x_j} = P_k - \beta^* \rho k \omega + \frac{\partial}{\partial x_j} \left[(\mu + \sigma_k \mu_t) \frac{\partial k}{\partial x_j} \right] \quad (5)$$

where P_k denotes the turbulence production rate due to viscous forces, represented by the time-averaged Reynolds stress and time-averaged velocity gradient:

$$P_k = \tau(u_i, u_j) \frac{\partial \bar{u}_i}{\partial x_j} \quad (6)$$

The ω equation is expressed as:

$$\frac{\partial(\rho \omega)}{\partial t} + \frac{\partial(\rho \bar{u}_j \omega)}{\partial x_j} = P_\omega - \beta \rho \omega^2 + \frac{\partial}{\partial x_j} \left[(\mu + \sigma_\omega \mu_t) \frac{\partial \omega}{\partial x_j} \right] + 2\rho(1 - F_1) \frac{\sigma_\omega}{\omega} \frac{\partial k}{\partial x_j} \frac{\partial \omega}{\partial x_j} \quad (7)$$

where P_ω denotes the specific turbulence dissipation rate, represented by the P_k and the eddy viscosity coefficient. This is expressed as:

$$P_\omega = \frac{\gamma}{\nu_t} P_k \quad (8)$$

$$\gamma = \gamma_1 F_1 + \gamma_2 (1 - F_1) \quad (9)$$

This turbulence model introduces a mixing function F_1 :

$$F_1 = \tanh(\arg_1^4), \arg_1 = \min \left(\max \left(\frac{\sqrt{k}}{\beta^* \omega y}, \frac{500\nu}{y^2 \omega} \right), \frac{4\rho k \sigma_\omega}{CD_{k\omega} y^2} \right) \quad (10)$$

$$CD_{k\omega} = \max \left(2\rho \sigma_\omega \frac{1}{\omega} \frac{\partial k}{\partial x_j} \frac{\partial \omega}{\partial x_j}, 10^{-10} \right) \quad (11)$$

Using the mixing function F_2 to modify the eddy viscosity coefficient:

$$F_2 = \tanh(\arg_2^2), \arg_2 = \max \left(\frac{2\sqrt{k}}{\beta^* \omega y}, \frac{500\nu}{y^2 \omega} \right) \quad (12)$$

Then, the eddy viscosity coefficient is:

$$\nu_t = \frac{a_1 k}{\max(a_1 \omega, S F_2)} \quad (13)$$

where k represents turbulence kinetic energy; ω represents turbulence frequency; ν_t denotes eddy viscosity coefficient; ν denotes kinematic viscosity; S is the strain tensor; and y is the distance to the nearest wall. The constant values involved in this turbulence model are: $a_1 = 0.31$, $\beta^* = 0.09$, $\beta = 0.075$, $\gamma_1 = 0.556$, $\sigma_k = 0.85$, $\sigma_\omega = 0.5$, $\gamma_2 = 0.44$, and $\sigma_{\omega 2} = 0.856$ [24].

2.2. Entropy Production Theory

Considering that water has a high specific heat capacity, the flow process in the pump-turbine can be considered an isothermal process [25,26]. Therefore, according to the second law of thermodynamics and ignoring the heat transfer effect, there is always a certain amount of mechanical energy loss due to dissipation and friction effects in mechanical procedures. This loss is converted into internal energy and cannot be reused, a process

that is irreversible and leads to an increase in entropy. Entropy production theory can quantitatively analyze the details of energy dissipation during the flow of pump-turbines.

The entropy production rate is determined as [27]:

$$\dot{S}_D''' = \frac{\dot{Q}}{T} \quad (14)$$

where \dot{Q} is the energy dissipation rate and T is the Kelvin temperature.

As for turbulence, the entropy production contains two components:

$$\dot{S}_D''' = \dot{S}_D''' + \dot{S}_{D'}''' \quad (15)$$

$$\dot{S}_D''' = \frac{2\mu_{eff}}{T} \left[\left(\frac{\partial \bar{u}_1}{\partial x_1} \right)^2 + \left(\frac{\partial \bar{u}_2}{\partial x_2} \right)^2 + \left(\frac{\partial \bar{u}_3}{\partial x_3} \right)^2 \right] + \frac{\mu}{T} \left[\left(\frac{\partial \bar{u}_2}{\partial x_1} + \frac{\partial \bar{u}_1}{\partial x_2} \right)^2 + \left(\frac{\partial \bar{u}_3}{\partial x_1} + \frac{\partial \bar{u}_1}{\partial x_3} \right)^2 + \left(\frac{\partial \bar{u}_2}{\partial x_3} + \frac{\partial \bar{u}_3}{\partial x_2} \right)^2 \right] \quad (16)$$

$$\dot{S}_{D'}''' = \frac{2\mu_{eff}}{T} \left[\left(\frac{\partial u'_1}{\partial x_1} \right)^2 + \left(\frac{\partial u'_2}{\partial x_2} \right)^2 + \left(\frac{\partial u'_3}{\partial x_3} \right)^2 \right] + \frac{\mu_{eff}}{T} \left[\left(\frac{\partial u'_2}{\partial x_1} + \frac{\partial u'_1}{\partial x_2} \right)^2 + \left(\frac{\partial u'_3}{\partial x_1} + \frac{\partial u'_1}{\partial x_3} \right)^2 + \left(\frac{\partial u'_2}{\partial x_3} + \frac{\partial u'_3}{\partial x_2} \right)^2 \right] \quad (17)$$

where \dot{S}_D''' refers to the direct dissipation term caused by time-averaged velocity; $\dot{S}_{D'}'''$ refers to the time-averaged velocity component of the indirect dissipation term caused by pulsating velocity; \bar{u}_1 , \bar{u}_2 , and \bar{u}_3 are the time-averaged velocity components; and u'_1 , u'_2 , and u'_3 are velocity fluctuation components. μ_{eff} represents the effective dynamic viscosity:

$$\mu_{eff} = \mu + \mu_t \quad (18)$$

where μ is the dynamic viscosity and μ_t is the eddy viscosity.

However, the velocity fluctuation component cannot be obtained by the RANS method. Kock et al. [28] and Mathieu et al. [29] proposed that the local entropy production rate caused by velocity fluctuations is related to ε or ω of the turbulence model. For the SST k - ω turbulence model, the indirect dissipation term of entropy production can be approximated as follows:

$$\dot{S}_{D'}''' = \beta \frac{\rho \omega k}{T} \quad (19)$$

where β is equal to 0.09 [30]. Many scholars who have adapted this formula for entropy production calculations have verified its validity [31–33].

Furthermore, because of the high velocity gradient near the wall region, a strong wall effect is caused, and thus, entropy is generated; the entropy production caused by wall shear stress should also be considered. Duan et al. [34] introduced a wall function with wide adaptability and better computational accuracy to calculate the entropy production near the wall region:

$$S_{pro,W} = \int_A \frac{\vec{\tau}_w \cdot \vec{v}_w}{T} dA \quad (20)$$

where $S_{pro,W}$ represents the entropy production rate caused by wall shear stress (EPWS) and $\vec{\tau}_w$ and \vec{v}_w represent the shear stress and velocity at the center of the first grid near the wall, respectively.

The entropy production rate caused by direct dissipation and turbulence dissipation can be obtained by volumetrically integrating \dot{S}_D''' and $\dot{S}_{D'}'''$ over the computational domain, respectively:

$$S_{pro,\bar{D}} = \int_V \dot{S}_D''' dV \quad (21)$$

$$S_{pro,D'} = \int_V \dot{S}_{D'}''' dV \quad (22)$$

where $S_{pro,\bar{D}}$ represents the entropy production rate caused by direct dissipation (EPDD) and $S_{pro,D'}$ represents the entropy production rate caused by turbulence dissipation (EPTD). Then, total entropy production rate (TEP) is:

$$S_{pro} = S_{pro,\bar{D}} + S_{pro,D'} + S_{pro,W} \quad (23)$$

As flow in the pump-turbine is considered an isothermal process, the rate of energy loss in the local volume is given as:

$$\dot{Q} = T \cdot S_{pro} \quad (24)$$

Energy loss can then be more intuitively expressed in terms of hydraulic loss:

$$h_{ep} = \frac{T \cdot S_{pro}}{\dot{m}g} \quad (25)$$

where h_{ep} represents the total hydraulic loss according to TEP and \dot{m} represents the mass flow rate. Correspondingly, h_{DD} , h_{TD} , and h_{WS} is the hydraulic loss caused by time-averaged velocity, turbulent pulse velocity, and wall effect, respectively.

2.3. Geometric Model

In this study, a prototype pump-turbine with a specific speed of 41 was investigated. The whole computational domain consisted of a draft tube, runner, guide vanes (GV), stay vanes (SV), and spiral casing. The entire pump-turbine computational domain is shown in Figure 1, and the schematic diagram depicting the position of these surfaces is shown in Figure 2. It should be noted that flow tubes have been attached at the draft tube inlet and spiral casing outlet, the lengths of which have been considerably extended to ensure a stable flow pattern in the inlet and outlet zones of the computational domain. The main design parameters of this prototype pump-turbine are listed in Table 1.

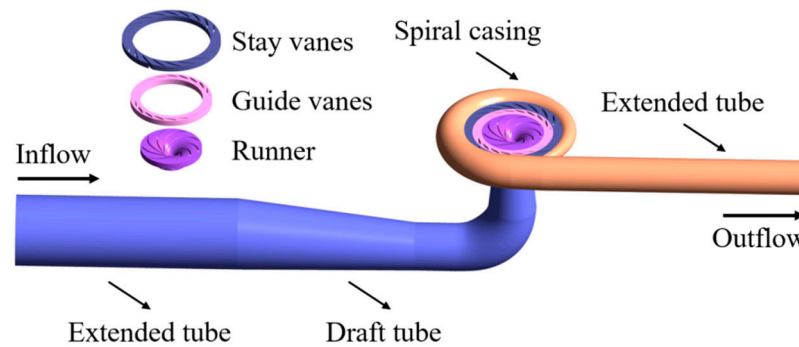


Figure 1. Entire computational domain of the prototype pump-turbine operated in pump mode.

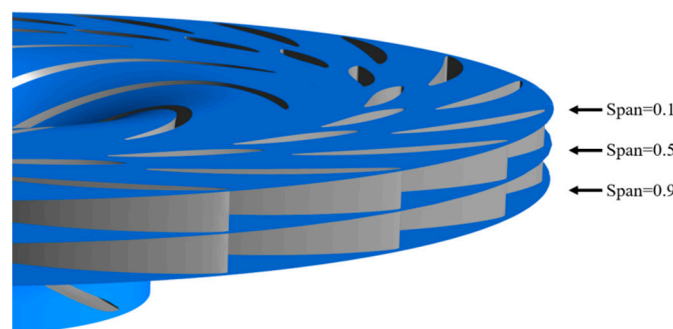


Figure 2. Spanwise position of the three selected planes through the runner, guide vane, and stay vane flow domains.

Table 1. Main parameters of the prototype pump-turbine operated in pump mode.

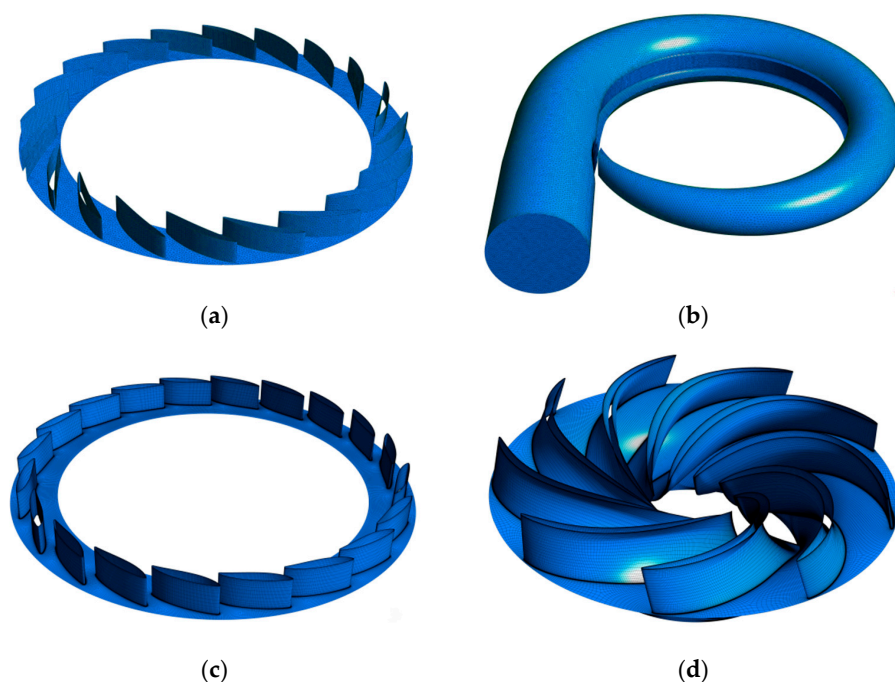
Parameter	Value
Runner inlet diameter D_1 /m	2.37
Runner outlet diameter D_2 /m	4.20
Number of runner blades	9
Number of guide-vanes	20
Specific speed n_q	41
Rated speed n_r /(rpm)	428.6
Rated working head H_r /m	442.82
Rated discharge Q_r /(m ³ /s)	61.87
Rated power input/(MW)	298.6

2.4. Grid Generation

The cell numbers and mesh quality for each of the fluid domain's components are listed in Table 2. Considering that mesh quality is a decisive factor in simulation accuracy, the global mesh quality for the entire domain did not fall below 3.3, and a fine mesh was generated in key regions, such as the runner and guide-vane channels, using commercial software ANSYS-TurboGrid. The grid generation component of the ANSYS software, ANSYS-ICEM, was used for the generation of mesh in all the remaining flow domains. As shown in Figure 3, a hybrid mesh was used in the stay-vane channels and spiral casing region, and a hexahedral structured mesh was used in the rest of zones. Globally, a well-refined mesh was generated within the boundary layers of all components.

Table 2. Details of three sets of grids.

Part	Mesh1		Mesh2		Mesh3	
	Nodes	Quality	Nodes	Quality	Nodes	Quality
Spiral casing with extended tube	4.20	0.68	82.7366	0.63	37.0997	0.62
Stay vanes	2.37	0.35	113.5939	0.33	50.7443	0.32
Guide vanes	9	0.57	279.7729	0.57	126.5364	0.56
Runner	20	0.33	381.3327	0.34	178.1229	0.34
Draft tube with extended tube	41	0.60	138.4717	0.60	59.305	0.59
Sum	428.6	-	995.9078	-	451.8083	-

**Figure 3.** A schematic of grid details: (a) stay vanes; (b) spiral casing; (c) guide vanes; and (d) runner.

2.5. Numerical Settings

For this prototype pump-turbine with its large size, the maximum Reynolds number could go up to 10^8 ($Re \approx 10^8$) when turbulent flow was fully developed. If the grid's y^+ value was adjusted to about 1, it would result in the need for a huge number of grids, thus consuming a massive amount of computational resources and not realistic or efficient for practice. In this paper, wall functions that could simulate the near-wall region were used to accurately describe the flow at the near-wall where viscous shear stresses dominated. The center of the first grid layer was arranged in the log-law region and the y^+ value at the runner blade and GV was in the range of 30~300. Accordingly, the near-wall region was suitable for high Reynolds number turbulence models, such as the $k-\varepsilon$ turbulence model.

As the standard $k-\varepsilon$ model is more demanding for the conditions of free turbulence, the shear pressure transport model SST $k-\omega$ was chosen to solve this problem. The model combined the advantages of the $k-\varepsilon$ and $k-\omega$ turbulence models [35]. It used the $k-\varepsilon$ model in the near-wall region and the $k-\omega$ model away from the wall [36]. The model takes into the transportation of turbulent shear stress to modify the turbulent viscosity, so it can avoid over-prediction of the vortex viscosity coefficient. Thus, it had higher simulation accuracy for free flow in the near-wall region and inverse pressure gradient flow.

The commercial software ANSYS Fluent 2021 was employed and the finite volume method was utilized to conduct the steady incompressible turbulent flow simulation of the pump-turbine in pump mode. The SST $k-\omega$ turbulence model was utilized and the SIMPLEC algorithm was selected as the pressure-velocity coupling method. The flow turbulence intensity at the inlet was 5%. In pump mode, mass flow rate at the extended tube of the draft tube was set as the inlet boundary condition, and the total pressure at the extended tube of the spiral casing was set as the outlet boundary condition and set to zero. No-slip wall conditions were set for all the walls. For convergence control, the RMS (root mean square) residual for each time step was set below 10^{-5} .

2.6. Grid Independence Validation

This research applied the Richardson extrapolation (RE) method to verify grid independence, and the grid convergence index (GCI) was used to quantitatively evaluate the convergence of the computational results [37–39]. As shown in Table 2, three sets of grids were generated to perform convergence analysis, and the number and scale of meshes proportionally decreased for the three sets of grids, based on the consistent meshing strategy. The mesh refinement factor r was defined as in Equation (21) [40]. According to the recommendation of the American Society of Mechanical Engineers (ASME), it should be greater than 1.3 [41]. Therefore, the three groups of grid numbers were set to 22.55 million, 9.96 million, and 4.52 million, respectively.

$$r = \frac{h_{coarse}}{h_{fine}}, h = \left[\frac{1}{N} \sum_{i=1}^N (\Delta V_i) \right]^{1/3} \quad (26)$$

where h_{coarse} denotes the size of the coarse grid and h_{fine} denotes the size of the fine grid.

Head and efficiency were selected as the variables for convergence analysis, and numerical simulations were carried out for all three groups of grids under optimal operating conditions. The results of the grid convergence analysis are shown in Table 3. Fine GCI values for both head and efficiency as evaluation variables were less than 3%, indicating that the grid met the convergence criteria. Considering the accuracy and computational cost of the simulation, the grid of 9.96 million was chosen for this study.

Table 3. Grid independence validation.

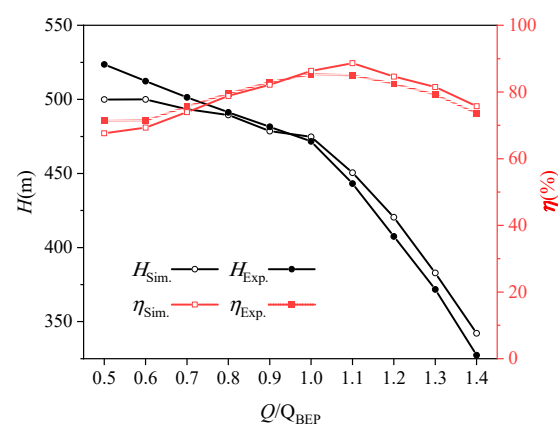
Parameter	$\varphi = H$ (m)	$\varphi = \eta$ (%)
N_1	22,553,199	
N_2	9,959,078	
N_3	4,518,083	
Mesh refinement factor r_{21}	1.3132	
Mesh refinement factor r_{32}	1.3014	
Numerical value φ_1	477.5352	87.1648
Numerical value φ_2	474.7498	86.3246
Numerical value φ_3	469.9528	84.9235
Apparent order p	2.11672	1.98787
Extrapolated value φ_{ext}^{21}	481.1052	88.3335
Relative error e_a^{21}	0.5833%	0.9638%
Extrapolated error e_{ext}^{21}	0.7421%	1.3231%
Grid convergence index GCI_{fine}^{21}	0.9344%	1.6761%

3. Results and Discussion

3.1. Experimental Validation

The model test of the pump-turbine was held at the hydraulic test rig of the Harbin Institute of Large Electrical Machinery. From the inlet of the draft tube extension tube to the outlet of the spiral casing extension tube, the entire flow path of the model pump-turbine was geometrically similar to that of the prototype pump-turbine, and there was a scale factor of 9.48 between the prototype and model pump-turbine.

The external characteristics of the prototype pump-turbine at the 132.72 mm guide vane opening (GVO), which were obtained based on model test data, were compared with the numerical simulation results. As shown in Figure 4, the water head H (m) and efficiency η (%) curves obtained from experiments and numerical simulations agreed relatively well, especially near the best efficiency point (BEP). At all operating points, the numerical simulation error in terms of the water head was less than 5%. In addition, under minimum flow conditions, the numerically measured efficiency presented an error of 5.22%, which was the highest of the entire investigated flow range, with all remaining operating points having numerical simulation efficiency errors smaller than 5%. The obtained results demonstrated that the chosen grid number and numerical simulation scheme were sufficiently reliable to ensure the credibility of the subsequent discussion and analysis.

**Figure 4.** Validation of the external characteristics at 132.72 mm guide vane opening.

To validate the reliability of the entropy production method, hydraulic losses h_{cp} obtained through the entropy production method were compared with the hydraulic losses

h_p obtained through the differential pressure method, based on experimental results. h_p was calculated by Equations (27)–(29).

$$H = \frac{\int_{In} p_{Tot} d\dot{m} - \int_{Out} p_{Tot} d\dot{m}}{\rho \dot{m} g} \quad (27)$$

$$P_t = \frac{nM}{9.55} \quad (28)$$

$$h_p = \frac{P_t}{\dot{m} g} - H \quad (29)$$

where H denotes delivery head; p_{Tot} denotes total pressure; P_t denotes total input power; and M indicates moment.

Figure 5 indicates that the total hydraulic losses significantly decreased, then gradually increased with the flow rate. The largest hydraulic losses occurred at minimum flow conditions ($0.5Q_{BEP}$), whereas the least hydraulic losses were recorded at the BEP. The hydraulic losses obtained by the entropy production method were consistent with the ones obtained by the differential pressure method. The maximum error between both methods (9.56%) was recorded under the largest flow rate ($1.4Q_{BEP}$). The hydraulic loss measurement error between the experiment and entropy production method at $0.5Q_{BEP}$ was 6.22%, and the error around the $1.0Q_{BEP}$ was approximately 4%. Therefore, we confirmed that the entropy production method was reliable in hydraulic losses calculations within pump-turbines.

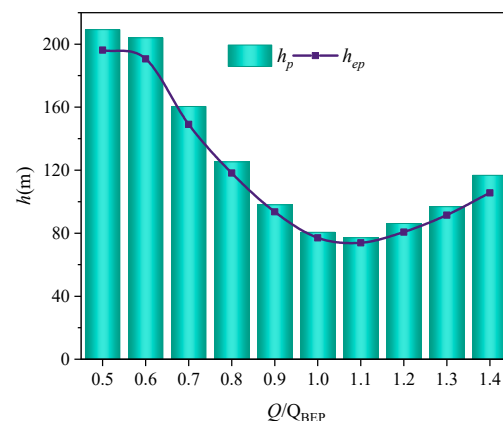


Figure 5. Hydraulic loss comparison between entropy production method and differential pressure method.

3.2. Analysis of Three Hydraulic Loss Compositions

The proportion and variation patterns of three entropy production terms corresponding to three hydraulic loss compositions are shown in Figures 6 and 7. The entropy production in the near-wall region mainly originated from the large velocity gradient caused by the shear stress between the first layer of the grid node and the wall, which could be approximated as friction loss. The contribution of the EPWS to the TEP was minimal, contributing about 1–2%, and varied slowly with different flow rates. The entropy production of the main flow region was primarily triggered by flow separation, backflow, and vortices formation. The entropy production in the main flow region was dominant, with the EPTD contributing the most to the TEP (about 50–61%) and the EPDD coming in second (about 37–48%). The entropy production in the mainstream region steeply increased with the decrease in flow rate when the flow rate was less than $1.0Q_{BEP}$, and the growth rate of entropy production slowed down after the flow rate decreased to $0.6Q_{BEP}$. When the flow rate was greater than $1.0Q_{BEP}$, the average velocity gradient grew and the turbulent velocity pulsation was significantly enhanced; with the EPTD sharply rising with the increase in

flow rate, and the EPDD increasing at a slower rate, significantly expanding the proportion of the EPTD in the TEP.

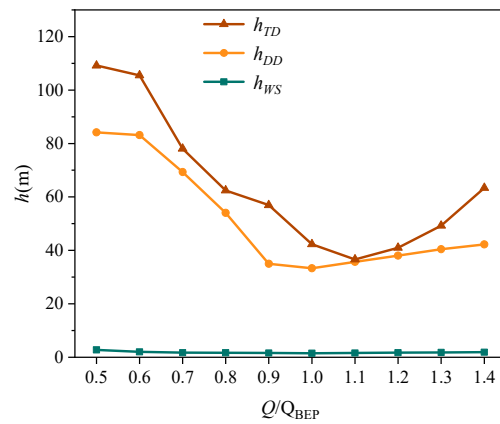


Figure 6. Evolution of each entropy production term under various operating points.

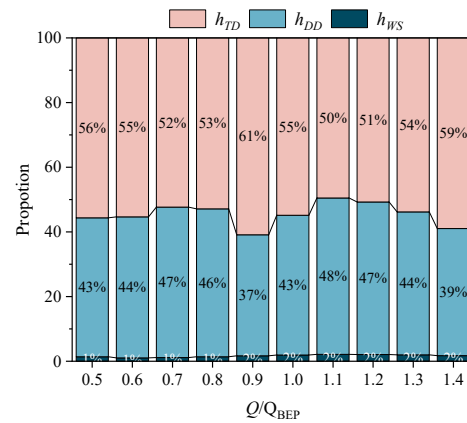


Figure 7. Proportions of each entropy production term under various operating points.

3.3. Analysis of Hydraulic Loss for Each Flowing Domain

As for different components of the pump-turbine computational domain, the TEP had different evolving trends as the flow rate changed. As shown in Figure 8, the TEP at the draft tube with its extended tube, GV, and SV decreases and then increases with a continuously increasing flow rate. The three components reached the minimum TEP value at $1.1Q_{BEP}$, $1.0Q_{BEP}$, and $0.9Q_{BEP}$, respectively. The TEP at the runner continuously decreased with flow rate increase, reaching its minimum value at $1.4Q_{BEP}$.

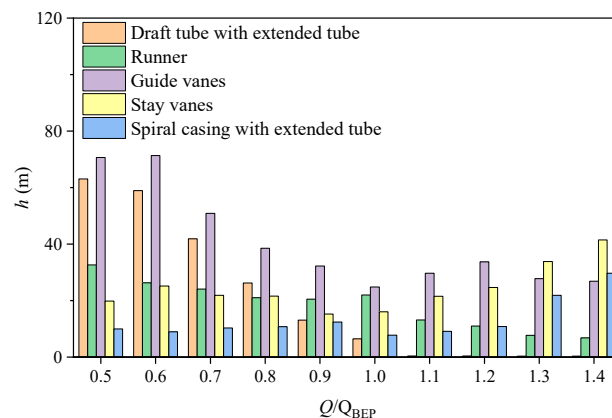


Figure 8. Changes of entropy production in each simulated domain.

The TEP at the draft tube and its extension sharply decreased for operating conditions in the range from $0.5Q_{BEP}$ (low-flow) to $1.0Q_{BEP}$ operating conditions. Then, it decreased to a small value and stayed stable (negligible variations) for the whole range of flow conditions in the over-flow zone. Within the GV flow domain, TEP first decreased from low-flow conditions, reaching its smallest value under BEP conditions, after which it fluctuated for the whole range of over-flow conditions. As for the TEP at the SV flow domain, there were random variations for the whole range of flows in the part-flow zone ($Q_i \leq Q_{BEP}$), reaching its maximum and minimum values at $0.6Q_{BEP}$ and $0.9Q_{BEP}$, respectively. In the over-flow zone ($Q_i > Q_{BEP}$), the SV's TEP continuously increased with the flowrate, reaching its peak value at $1.4Q_{BEP}$. The TEP in the runner flow domain first decreased until $0.9Q_{BEP}$, before slightly increasing to $1.0Q_{BEP}$, then continuously decreasing in the over-flow zone. For the whole range of tested flow conditions from part-flow ($Q_i \leq Q_{BEP}$) through full-flow ($1.0Q_{BEP}$) to over-flow conditions ($Q_i > Q_{BEP}$), GV and SV flow domains experienced the largest entropy production, followed by the runner. The entropy production within the draft tube was greater under low-flow conditions, whereas that of the spiral casing was greater under high-flow conditions. As the flow rate increased, the flow impact was enhanced at the spiral casing, resulting in increased hydraulic losses. When water flowed through the SV and GV into the runner and draft tube, the flow became uniform and hydraulic losses decreased.

3.4. Distribution and Variation of Entropy Production

To learn the evolution mechanism of different flow field characteristics with the changing machine influx, three flow conditions have been selected for further analysis, namely the low-flow condition ($0.6Q_{BEP}$), BEP flow condition ($1.0Q_{BEP}$), and high-flow condition ($1.4Q_{BEP}$). Different flow field details, such as the velocity-colored streamlines, pressure contours, turbulent kinetic energy (TKE) contours, as well as the EPTD and EPDD contours at different flow domains (runner, GV, and SV), are shown in Figures 9–11. Three surfaces in the span-wise direction from the hub to the shroud were analyzed.

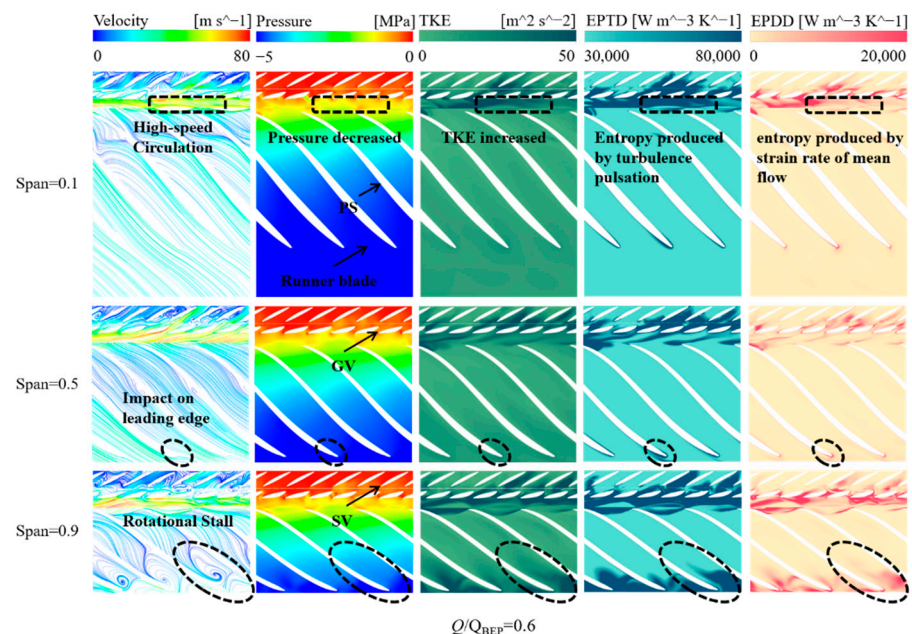


Figure 9. Distribution of entropy production under low-flow conditions ($0.6Q_{BEP}$).

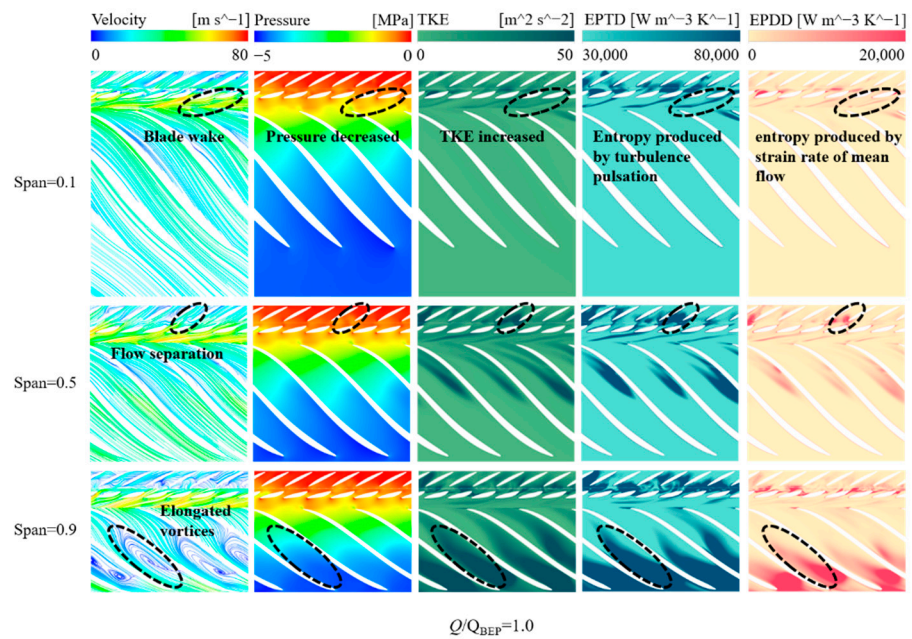


Figure 10. Distribution of the entropy production under BEP conditions ($1.0Q_{BEP}$).

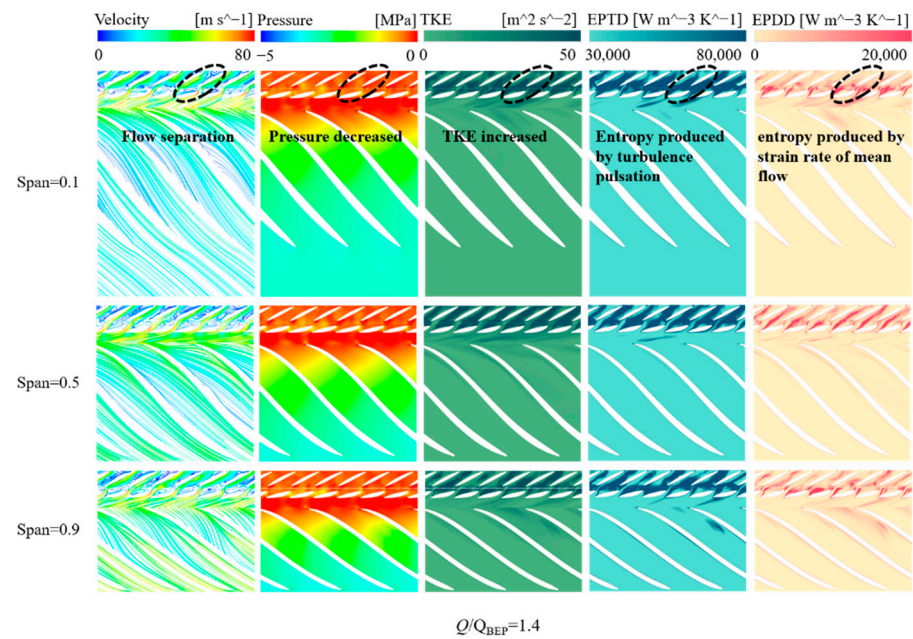


Figure 11. Entropy production distribution under high-flow conditions ($1.4Q_{BEP}$).

The entropy production of the near-wall region was tiny and relatively close for different flow conditions. Therefore, the hydraulic loss of the pump-turbine at the pump mode primarily originated from the poor flow in the mainstream region. The EPDD and EPTD reflect the local entropy production rate due to the average velocity gradient and fluctuating velocities, respectively. As seen in Figures 9–11, the distributions of EPDD and EPTD are in high agreement with the distribution of TKE. The significant mean velocity gradient in the unsteady flow zones caused an increase in EPDD and led to an increase in turbulent velocity pulsation. Therefore, the TKE increased; meanwhile, the turbulent dissipation rate correspondingly increased, causing an increase in EPTD. It should be noted that the turbulent velocity pulsations were influenced both by the velocity gradient and intensity of convective flow. In general, high local entropy production rates were found in large-scale vortex regions, wall flow separation regions, and rotational stall regions.

As for low-flow conditions ($0.6Q_{BEP}$), the entropy production at span 0.1 was mainly concentrated within the GV flow channels and runner blade's leading edge. High entropy production areas at span 0.5 were mainly located at the pressure surface of the runner blade near the leading edge, the blade wake region, and flow channels in the GV and SV flow domains. The entropy production at span 0.9 was primarily situated within all the GV flow channels, as well as the vaneless region. Furthermore, large-scale vortices occurred at the runner blade flow channels and caused high entropy production. This was because, as the flow rate decreased, the relative velocity of the intermediate flow surface also dropped and the inlet flow angle grew. This led to the stagnation point moving to the blade's pressure surface. When the inlet flow angle exceeded a certain value, flow separation occurred at the suction surface, generating vortices and forming stall masses. The static pressure in the rotating stall region was much lower than that of the surrounding zone. The vortex appeared in the same rotational direction as the runner; at the same time, a secondary vortex rotating in the opposite direction appeared at the exit of the inter-blade flow channels. These vortices would expand until the entire flow channel was blocked, resulting in the former runner blade impulse angle decreasing and latter blade impulse angle increasing. This resulted in the stagnation point moving from the trailing edge of the blade to the pressure surface, so that, from the former runner blade flow channel to the latter one, the vortex was shifted from the direction of the runner inlet side to the direction of the runner outlet side.

In addition, some of the SV flow channels had high entropy production areas. This was due to flow separation in some SV flow channels, resulting in the formation of separation vortices, which in turn blocked the SV flow channels, resulting in larger flow velocity in adjacent flow channels. The intense momentum exchange between the low-velocity region of the separation vortex and high velocity region of the adjacent flow channel resulted in high hydraulic losses, and higher local entropy production characteristics were correspondingly exhibited.

As for BEP conditions ($1.0Q_{BEP}$), the angle between the direction of the water flow and blade placement was smaller; therefore, the flow separation was weaker [42], resulting in smaller hydraulic losses. At span 0.1, the flow in the runner inter-blade flow channels was pretty uniform; slight entropy production could only be found on the blade pressure surface. At span 0.5, a small amount of entropy production occurred in the runner blade flow channels near the pressure surface. At span 0.9, elongated vortices existed in the runner blade flow channels near the runner inlet, and generated a comparatively large zone of high entropy production areas. The increase in the vortices caused an increase in the TKE and led to a higher velocity gradient, resulting in a higher entropy production rate. Additionally, the flow separation in the flow channels between GV and SV, as well as the recorded blade wakes, led to entropy production on the three surfaces.

Regarding high-flow conditions ($1.4Q_{BEP}$), for all three span-wise surfaces, the flow in the runner inter-blade flow channels was uniform and the hydraulic losses were extremely small, with only a small number of hydraulic losses seen at the blade pressure surface in the direction of the hub. Regions of high entropy production were mainly found in the inter-guide vane and inter-stay vane flow channels. For high-flow conditions, the flow impacted the GV inlet side, triggering flow separation and many small-scale vortices distributed along the circumferential direction, causing differential pressure in certain areas. Due to the spatial compactness and complexity of the flow passages within the GV and SV domains, these unstable flows were difficult to develop and dissipate rapidly. The swirling flows that appeared within the inter-guide vane flow passages also affected the flow stability in the SV passage in convection, leading to significant hydraulic losses in both the GV and SV flow channels.

In general, most of hydraulic losses occurred within the inter-guide vane flow passages, vaneless space region, and runner inlet zone. These hydraulic losses were also found to significantly increase span-wise from the hub toward the shroud side. Under BEP conditions, hydraulic losses mainly occurred within the runner inter-blade flow channels

near the runner inlet zone, in the direction of the runner shroud. More losses occurred in the blade wake regions, as well as the flow channels between guide vanes and stay vanes. Small hydraulic losses could also be seen within the draft tube, spiral casing, and respective extensions. When the machine flow conditions deviated from the BEP, hydraulic losses at the GV and SV sharply increased and occupied a dominant position. As for low-flow conditions, high hydraulic losses primarily occurred in the GV flow channels and the draft tube. Secondly, hydraulic losses occurred in some of the SV flow channels, vaneless region, runner inter-blade flow channels near the runner inlet zone in the direction of the runner shroud, and blade wake regions. Under high-flow conditions, high hydraulic losses were mostly concentrated in the middle of the SV flow channels, GV wake regions, and the spiral casing. Secondly, the runner blade pressure surface in the vicinities of the hub side also had a small number of hydraulic losses.

4. Conclusions

We adopted the entropy production theory to investigate the composition and distribution of hydraulic losses under different flow conditions for a pump-turbine prototype, operating in pump mode. The following conclusions were drawn:

1. As the flow rate increased, the total hydraulic losses significantly decreased, before gradually increasing with the flow rate. Generally, recorded hydraulic losses through the whole flow passage were primarily caused by flow separations, backflows, and vortices. In the near-wall regions, they could be approximated as friction losses. Three types of entropy production exhibited the same variation pattern as the TEP. EPTD and EPDD were dominant, with EPTD contributing the most to TEP, followed by EPDD. The TEP at the draft tube, GV, SV, and the spiral casing followed the aforementioned variation pattern of the total hydraulic losses, but the TEP at the runner continuously decreased as flow rate increased.
2. The location and distribution mode of high hydraulic losses along the pump-turbine's full flow passage significantly depended on the machine flow conditions. Under low-flow conditions, high hydraulic losses occurred primarily in the GV and draft tube flow domains. On the other hand, under high-flow rate conditions, high hydraulic losses were mostly concentrated in SV, the spiral casing, and GV;
3. The pump-turbine hydraulic losses in pump mode primarily originated from the poor flow state in the mainstream region, and they significantly increased in the span-wise direction from the hub to the shroud side. Under low-flow conditions, hydraulic losses mainly came from flow separations in the GV flow channels, vortices in the vaneless region, and flow shocks on the runner blade's leading edge. Under high-flow conditions, hydraulic losses mostly originated from the flow separations that took place within the flow channels in GV and SV flow domains, GV wake flows, and unsteady flows within the spiral casing. As to BEP, the hydraulic losses mainly derived from the vortices in flow channels between GV and SV, the blade wakes, and the elongated vortices in the runner's inter-blade flow channels near the shroud side.

Author Contributions: Conceptualization, X.Y. and K.K.; methodology, X.Y.; software, X.Y.; validation, X.Y., K.K. and H.C.; formal analysis, X.Y.; investigation, X.Y.; resources, Y.Z.; data curation, X.Y.; writing—original draft preparation, X.Y.; writing—review and editing, X.Y., K.K. and M.B.; visualization, X.Y.; supervision, K.K. and Y.Z.; project administration, K.K. and Y.Z.; funding acquisition, K.K., H.C. and Y.Z. All authors have read and agreed to the published version of the manuscript.

Funding: This study was supported by the National Natural Science Foundation of China (52009033; 52006053), the Natural Science Foundation of Jiangsu Province (BK20200509; BK20200508); and the Postdoctoral Research Foundation of China (2022T150185; 2022M711021; 2021M690876). We also gratefully acknowledge the support of Hohai University, China.

Data Availability Statement: Not applicable.

Conflicts of Interest: The authors declare no conflict of interest.

Nomenclature

i, j, k	Indices denoting the x, y, and z directions
$\bar{u}_1, \bar{u}_2, \bar{u}_3$	Time-averaged velocity components
x_1, x_2, x_3	Cartesian coordinate component(m)
u'_1, u'_2, u'_3	Velocity fluctuation components (m/s)
ρ	Density (kg/m ³)
t	Physical time (s)
\bar{P}	Time average pressure (Pa)
μ	Dynamic viscosity (Pa·s)
τ_{ij}	Subgrid-scale stress
∇	Hamilton operator
P_k	Turbulence production rate due to viscous forces
P_ω	Specific turbulence dissipation rate
k	Turbulence kinetic energy (m ² /s ²)
ω	turbulence frequency (s ⁻¹)
μ_{eff}	Effective dynamic viscosity (Pa·s)
μ_t	Turbulent viscosity (Pa·s)
ν	Kinematic viscosity (m ² /s)
ν_t	Eddy viscosity (m ² /s)
S	Strain tensor (s ⁻¹)
y	Distance to the nearest wall
y^+	Dimensionless wall distance
\dot{Q}	Energy dissipation rate
\dot{S}_{pro}	Total entropy production (W/K)
$\dot{S}_{\bar{D}}'''$	Entropy production rate caused by direct dissipation (W·m ⁻³ ·K ⁻¹)
$\dot{S}_{D'}'''$	Entropy production rate caused by turbulence dissipation (W·m ⁻³ ·K ⁻¹)
\dot{S}_W'''	Entropy production rate caused by wall shear stress(W·m ⁻² ·K ⁻¹)
T	Temperature (K)
$\vec{\tau}_w$	Velocity near the wall (m/s)
\vec{v}_w	Shear stress near the wall (Pa)
h_{ep}	Hydraulic loss obtained by entropy production method (m)
h_p	Hydraulic loss obtained by differential pressure method (m)
g	Gravity acceleration (m/s ²)
\dot{m}	Mass flow rate (kg/s)
r	Mesh refinement factor
h_{coarse}	Size of the coarse grid
h_{fine}	Size of the fine grid
H	Delivery head (m)
p_{Tot}	Total pressure (Pa)
M	Torque of the impeller blades (N·m)
n	Rotational speed (r/min)
P_t	Total input power (W)
Q	Flow rate (m ³ /s)
η	Pump efficiency (%)

Abbreviations

PIV	Particle Image Velocimetry
DNS	Direct Numerical Simulation
LES	Large Eddy Simulation
RANS	Reynolds-Averaged Navier-Stokes
EPDD	Entropy Production Rate caused by Direct Dissipation
EPTD	Entropy Production Rate caused by Turbulence Dissipation
EPWS	Entropy Production Rate caused by Wall Shear stress
TEP	Total Entropy Production
GV	Guide Vanes
SV	Stay Vanes
SST	Shear Stress Transport
SIMPLEC	Semi-Implicit Method for Pressure-Linked Equations-Consistent
RMS	Root Mean Square
RE	Richardson Extrapolation
GCI	Grid Convergence Index
ASME	American Society of Mechanical Engineers
GVO	Guide Vane Opening
BEP	Best Efficiency Point

References

- Li, D.; Zuo, Z.; Wang, H.; Liu, S.; Wei, X.; Qin, D. Review of positive slopes on pump performance characteristics of pump-turbines. *Renew. Sustain. Energy Rev.* **2019**, *112*, 901–916. [CrossRef]
- Shi, L.; Zhang, W.; Jiao, H.; Tang, F.; Wang, L.; Sun, D.; Shi, W. Numerical simulation and experimental study on the comparison of the hydraulic characteristics of an axial-flow pump and a full tubular pump. *Renew. Energy* **2020**, *153*, 1455–1464. [CrossRef]
- Lin, T.; Zhu, Z.; Li, X.; Li, J.; Lin, Y. Theoretical, experimental, and numerical methods to predict the best efficiency point of centrifugal pump as turbine. *Renew. Energy* **2021**, *168*, 31–44. [CrossRef]
- Kan, K.; Chen, H.; Zheng, Y.; Zhou, D.; Binama, M.; Dai, J. Transient characteristics during power-off process in a shaft extension tubular pump by using a suitable numerical model. *Renew. Energy* **2021**, *164*, 109–121. [CrossRef]
- Li, D.; Chang, H.; Zuo, Z.; Wang, H.; Li, Z.; Wei, X. Experimental investigation of hysteresis on pump performance characteristics of a model pump-turbine with different guide vane openings. *Renew. Energy* **2020**, *149*, 652–663. [CrossRef]
- Lu, G.; Zuo, Z.; Sun, Y.; Liu, D.; Tsujimoto, Y.; Liu, S. Experimental evidence of cavitation influences on the positive slope on the pump performance curve of a low specific speed model pump-turbine. *Renew. Energy* **2017**, *113*, 1539–1550. [CrossRef]
- Sun, Y.K.; Zuo, Z.G.; Liu, S.H.; Liu, J.T.; Wu, Y.L. Experimental Study of pressure fluctuations of a pump-turbine in transient period. In *Advanced Materials Research*; 2012; pp. 896–899. Available online: <https://www.scientific.net/AMR.516-517.896> (accessed on 1 October 2022).
- Han, Y.; Tan, L. Influence of rotating speed on tip leakage vortex in a mixed flow pump as turbine at pump mode. *Renew. Energy* **2020**, *162*, 144–150. [CrossRef]
- Kan, K.; Yang, Z.; Lyu, P.; Zheng, Y.; Shen, L. Numerical study of turbulent flow past a rotating axial-flow pump based on a level-set immersed boundary method. *Renew. Energy* **2021**, *168*, 960–971. [CrossRef]
- Liu, Y.; Tan, L. Tip clearance on pressure fluctuation intensity and vortex characteristic of a mixed flow pump as turbine at pump mode. *Renew. Energy* **2018**, *129*, 606–615. [CrossRef]
- Wang, C.; Zhang, Y.; Yuan, Z.; Ji, K. Development and application of the entropy production diagnostic model to the cavitation flow of a pump-turbine in pump mode. *Renew. Energy* **2020**, *154*, 774–785. [CrossRef]
- Wang, W.; Tai, G.; Pei, J.; Pavesi, G.; Yuan, S. Numerical investigation of the effect of the closure law of wicket gates on the transient characteristics of pump-turbine in pump mode. *Renew. Energy* **2022**, *194*, 719–733. [CrossRef]
- Tao, R.; Wang, Z. Comparative numerical studies for the flow energy dissipation features in a pump-turbine in pump mode and turbine mode. *J. Energy Storage* **2021**, *41*, 102835. [CrossRef]
- Shi, L.; Zhu, J.; Tang, F.; Wang, C. Multi-disciplinary optimization design of axial-flow pump impellers based on the approximation model. *Energies* **2020**, *13*, 779. [CrossRef]
- Gan, X.; Pavesi, G.; Pei, J.; Yuan, S.; Wang, W.; Yin, T. Parametric investigation and energy efficiency optimization of the curved inlet pipe with induced vane of an inline pump. *Energy* **2022**, *240*, 122824. [CrossRef]
- Ji, L.; Li, W.; Shi, W.; Tian, F.; Agarwal, R. Effect of blade thickness on rotating stall of mixed-flow pump using entropy generation analysis. *Energy* **2021**, *236*, 121381. [CrossRef]
- Yu, Z.-F.; Yan, Y.; Wang, W.-Q.; Liu, X.-S. Entropy production analysis for vortex rope of a Francis turbine using hybrid RANS/LES method. *Int. Commun. Heat Mass Transf.* **2021**, *127*, 105494. [CrossRef]
- Zhang, F.; Appiah, D.; Hong, F.; Zhang, J.; Yuan, S.; Adu-Poku, K.A.; Wei, X. Energy loss evaluation in a side channel pump under different wrapping angles using entropy production method. *Int. Commun. Heat Mass Transf.* **2020**, *113*, 104526. [CrossRef]

19. Gong, R.; Wang, H.; Chen, L.; Li, D.; Zhang, H.; Wei, X. Application of entropy production theory to hydro-turbine hydraulic analysis. *Sci. China Technol. Sci.* **2013**, *56*, 1636–1643. [[CrossRef](#)]
20. Hou, H.; Zhang, Y.; Li, Z. A numerically research on energy loss evaluation in a centrifugal pump system based on local entropy production method. *Therm. Sci.* **2017**, *21*, 1287–1299. [[CrossRef](#)]
21. Li, D.; Wang, H.; Qin, Y.; Han, L.; Wei, X.; Qin, D. Entropy production analysis of hysteresis characteristic of a pump-turbine model. *Energy Convers. Manag.* **2017**, *149*, 175–191. [[CrossRef](#)]
22. Qin, Y.; Li, D.; Wang, H.; Liu, Z.; Wei, X.; Wang, X. Investigation on hydraulic loss component and distribution in hydraulic machinery: A case study of pump-turbine in pump mode. *J. Energy Storage* **2022**, *52*, 104932. [[CrossRef](#)]
23. Pope, S.B.; Pope, S.B. *Turbulent Flows*; Cambridge University Press: Cambridge, UK, 2000.
24. Wang, Y.; Wang, W. Applicability of eddy viscosity turbulence models in low specific speed centrifugal pump. *Proc. IOP Conf. Ser. Earth Environ. Sci.* **2012**, *15*, 062013. [[CrossRef](#)]
25. Wang, W.; Pavesi, G.; Pei, J.; Yuan, S. Transient simulation on closure of wicket gates in a high-head Francis-type reversible turbine operating in pump mode. *Renew. Energy* **2020**, *145*, 1817–1830. [[CrossRef](#)]
26. Lin, T.; Li, X.; Zhu, Z.; Xie, J.; Li, Y.; Yang, H. Application of enstrophy dissipation to analyze energy loss in a centrifugal pump as turbine. *Renew. Energy* **2021**, *163*, 41–55. [[CrossRef](#)]
27. Bejan, A. *Entropy Generation Minimization: The Method of Thermodynamic Optimization of Finite-Size Systems and Finite-Time Processes*; CRC Press: Boca Raton, FL, USA, 2013.
28. Kock, F.; Herwig, H. Local entropy production in turbulent shear flows: A high-Reynolds number model with wall functions. *Int. J. Heat Mass Transf.* **2004**, *47*, 2205–2215. [[CrossRef](#)]
29. Mathieu, J.; Scott, J. *An Introduction to Turbulent Flow*; Cambridge University Press: Cambridge, UK, 2000.
30. Menter, F.R. Two-equation eddy-viscosity turbulence models for engineering applications. *AIAA J.* **1994**, *32*, 1598–1605. [[CrossRef](#)]
31. Wang, C.; Zhang, Y.; Hou, H.; Zhang, J.; Xu, C. Entropy production diagnostic analysis of energy consumption for cavitation flow in a two-stage LNG cryogenic submerged pump. *Int. J. Heat Mass Transf.* **2019**, *129*, 342–356. [[CrossRef](#)]
32. Yu, Z.-F.; Wang, W.-Q.; Yan, Y.; Liu, X.-S. Energy loss evaluation in a Francis turbine under overall operating conditions using entropy production method. *Renew. Energy* **2021**, *169*, 982–999. [[CrossRef](#)]
33. Kan, K.; Zhang, Q.; Xu, Z.; Zheng, Y.; Gao, Q.; Shen, L. Energy loss mechanism due to tip leakage flow of axial flow pump as turbine under various operating conditions. *Energy* **2022**, *255*, 124532. [[CrossRef](#)]
34. Duan, L.; Wu, X.; Ji, Z.; Xiong, Z.; Zhuang, J. The flow pattern and entropy generation in an axial inlet cyclone with reflux cone and gaps in the vortex finder. *Powder Technol.* **2016**, *303*, 192–202. [[CrossRef](#)]
35. Menter, F.R. Review of the shear-stress transport turbulence model experience from an industrial perspective. *Int. J. Comput. Fluid Dyn.* **2009**, *23*, 305–316. [[CrossRef](#)]
36. Davidson, L. *Fluid Mechanics, Turbulent Flow and Turbulence Modeling*; Chalmers University of Technology: Goteborg, Sweden, 2018.
37. Stern, F.; Wilson, R.V.; Coleman, H.W.; Paterson, E.G. Comprehensive approach to verification and validation of CFD simulations—part 1: Methodology and procedures. *J. Fluids Eng.* **2001**, *123*, 793–802. [[CrossRef](#)]
38. Roy, C.J. Grid convergence error analysis for mixed-order numerical schemes. *AIAA J.* **2003**, *41*, 595–604. [[CrossRef](#)]
39. Trivedi, C.; Cervantes, M.J.; Gandhi, B.K. Investigation of a high head Francis turbine at runaway operating conditions. *Energies* **2016**, *9*, 149. [[CrossRef](#)]
40. Celik, I.B.; Ghia, U.; Roache, P.J.; Freitas, C.J. Procedure for estimation and reporting of uncertainty due to discretization in CFD applications. *J. Fluids Eng.-Trans. ASME* **2008**, *130*, 078001.
41. Kan, K.; Xu, Z.; Chen, H.; Xu, H.; Zheng, Y.; Zhou, D.; Muhirwa, A.; Maxime, B. Energy loss mechanisms of transition from pump mode to turbine mode of an axial-flow pump under bidirectional conditions. *Energy* **2022**, *257*, 124630. [[CrossRef](#)]
42. Liu, Y.; Li, X.; Lin, Z.; Li, L.; Zhu, Z. Numerical analysis of thermo-sensitive cavitating flows with special emphasises on flow separation and enstrophy conversion. *Int. Commun. Heat Mass Transf.* **2021**, *125*, 105336. [[CrossRef](#)]